ACS OMEGA

http://pubs.acs.org/journal/acsodf

Article

Synthesis of 2D Metal−Organic Nanosheets (MONs) by Liquid Phase Exfoliation: Applications in Effective Delivery of Antiulcer Drugs and Selective Adsorption and Removal of Cationic Dyes

Khalil M. A. Qasem,[▽] Shabnam Khan,[▽] M. Shahid,[*] Hatem A. M. Saleh, Younes S. A. Ghanem, Mohsen T. A. Qashqoosh, and Musheer Ahmad

Cite This: *ACS Omega* 2023, 8, 12232−12245

Read Online

ACCESS | Metrics & More | Article Recommendations | Supporting Information

ABSTRACT: Nowadays, the fabrication of 2D metal−organic nanosheets (2D MONs) has entered the research arena fascinating researchers worldwide. However, a lack of efficient and facile methods has remained a bottleneck for the manufacturing of these 2D MONs. Herein, a 2D metal−organic framework (MOF), i.e., 2D Cu-MOF, was synthesized using a facile and convenient stirring method by using 4,4′-trimethylenedipyridine (TMDP) as an organic linker. The as-prepared MOF was characterized in detail and based on single crystal X-ray diffraction analysis, it was established that tangled layers in the 2D Cu-MOF are interconnected to produce thick strands. These tangled layers could be easily separated via ultrasonication-induced liquid phase exfoliation (UILPE) to give the 2D Cu-MON as illustrated through Tyndall light scattering and exhaustive microscopic exploration such as scanning electron microscopy (SEM) and transmission electron microscopy (TEM). The application of this 2D Cu-MON was assessed in the field of drug delivery revealing exceptional drug loading for the drug lansoprazole (LPZ) by 2D Cu-MONs as well as drug release in the acidic and neutral medium demonstrating that the 2D Cu-MON is an excellent carrier for antiulcer drug delivery. For environmental protection, the application of 2D Cu-MON was also examined toward the removal of various cationic and anionic dyes with excellent selectivity toward cationic dye removal. The plausible mechanism for dye removal indicated the involvement of cation−π and $\pi-\pi$ interactions, for the effective adsorption of cationic dyes as well as a increase in the surface area of 2D Cu-MON by UILPE. Remarkably, the high drug loading and dye removal are imputed to the increase in surface area by UILPE. In a nutshell, the developed 2D Cu-MON will prove to be beneficial for application in the field of drug delivery as well as for wastewater treatment.

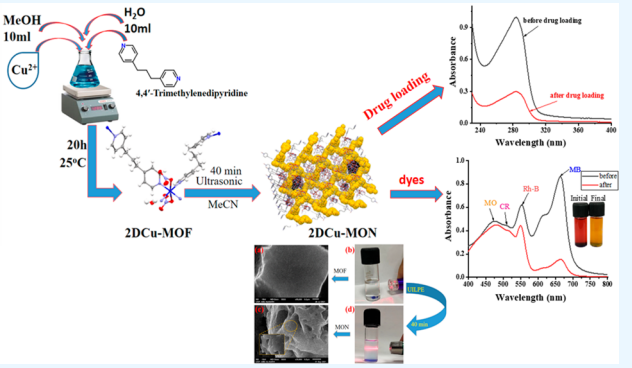

1. INTRODUCTION

Two-dimensional (2D) nanomaterials with distinct structure as well as intriguing physical and chemical properties hasve sparked the interest of researchers since the mechanical exfoliation of graphene from graphite was achieved in the year 2004.[1,2] Several graphene analogues, such as graphene oxide,[3] hexagonal boron nitride,[4] transition metal dichalcogenides,[5] graphitic carbon nitride,[6] noble metal nanosheets,[7,8] and covalent organic frameworks[9] have been developed up to this point enriching the family of 2D nanomaterials. Nowadays, the fabrication of 2D metal−organic nanosheets (2D MONs), a new category of crystalline porous materials constructed by linking organic ligands with metal nodes (e.g., metal ions/nodes), have attracted considerable research interest.[10] Some interesting features of MONs such as structural and functional tunability, ample active sites, extended lateral dimension, and high porosity make them efficient candidates in the fields of gas separation,[11] catalysis,[12−14] sensing,[15] drug delivery,[16,17] dye removal,[18] and much more. However, it is difficult to synthesize 2D MONs because the growth of the crystals is a limiting issue. Nowadays, several synthetic methodologies for the development of 2D MONs have been reported including top-down and bottom-up methods.[19] The top-down approach as the name suggests involves separation of nanosheets from a layered material. Basically, the layers/nanosheets in the bulk MOF are stacked on top of each other through a number of interactions, i.e., van der Waals forces, $\pi-\pi$ interactions, weak and strong hydrogen bonds, etc.[20] These interactions could be overcome by exfoliation methods such as mechanical exfoliation, sonication, and chemical exfoliation.[21] The

Received: December 29, 2022
Accepted: March 13, 2023
Published: March 23, 2023

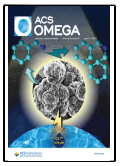

application of external stimuli including heat, light, solvent, and mechanochemical force cause the dimensional transition from 3D layered MOFs to 2D MONs without any loss of crystallinity.[22]

The high surface area of MONs is one of the interesting features which enables better interaction of MONs with guest molecules like drugs, dye molecules, and much more. Owing to their high surface area along with tunable structure, the MONs are potential carriers in the field of drug delivery allowing better drug interactions and high drug loading.[23] During the past few years, various metal−organic frameworks (MOFs) have been utilized for the purpose of drug encapsulation. Some of the most common drugs investigated to date are ibuprofen and anticancer drugs (doxorubicin, 5-fluorouracil, and cisplatin). In addition to these drugs, a drug named lansoprazole (LPZ) as illustrated in Figure 1, which is

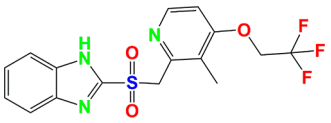

Figure 1. Chemical structure of drug lansoprazole (LPZ).

frequently used to treat peptic ulcers in a number of situations such as duodenal ulcers, benign gastric ulcers, gastroesophageal reflux disease, and also long-term Zollinger−Ellison syndrome, is of considerable research interest. Since the liver is the organ that metabolizes this medication most efficiently,[24] patients with renal and hepatic issues must take a lower dose. However, in some typical systems, a lower dose may not have the desired pharmacological effect. Regular use of LPZ has been linked to side effects include diarrhea, faintness, bellyache, body rashes, angioedema, impotence, thrombocytopenia, and much more. Owing to these severe side effects, LPZ delivery at the optimal concentration by using appropriate materials is quite necessary.[25] In this regard, designing materials with high payloads of LPZ, which is a proton-pump inhibitor used to minimize the production of acid in the stomach, is desirable. Hence, the application of this new category of MOF, i.e., 2D MONs in the field of drug delivery could serve the purpose.

Additionally, because of broad industrial expansion, it is becoming increasingly difficult for environmental chemists to remove harmful organic dye pollutants from wastewater.[26,27] Numerous enterprises discharge their effluent in urban neighborhoods that are directly connected to numerous groundwater sources. Wastewater contamination especially aromatic pollutants can easily contaminate subterranean water harming both the environment and human health.[28] Stable chemicals that do not break down readily in living tissue are the major problem because they either directly or indirectly impair human health and the health of other living things. As a result, they must be effectively dealt with as these can be harmful to drinking water even at very low amounts. The most stable chemicals are those that contain chlorine, heavy metal ions, organic molecules, and aromatic dyes.[29,30] Due to their negative effects on aquatic life, organic dyes rank as the third most serious water pollution.[31] Although dyes are predominantly utilized in the textile industry, they are also widely used to color a wide range of materials including papers, rubber, wood, plastic, and leather.[32] As a result, it is essential to eliminate all of these dangerous aromatic dyes from wastewater which is a significant issue. Numerous methods such as ozonization, photodegradation, coagulation, filtration, biosorption, and adsorption have been investigated for the removal of organic contaminants from an aquatic environment.[33] However, the adsorption technique has emerged as one of the most successful ones because of its simple handling, environmental friendliness, high adsorption effectiveness, low cost, and ability of adsorbent to be reused.[34,35] To specifically remove organic pollutants from wastewater, multiple environmental chemists investigated various adsorbents, including biomass, resin, activated carbon, clay, and zeolite materials.[36] Furthermore, organic dyes are difficult to remove from these materials due to their weak adsorption effectiveness.[37] In this aspect, MONs could be employed for the removal of aromatic dye molecules from wastewater by virtue of their high surface area with extended lateral dimensions along with the presence of specific noncovalent contacts such as electrostatic interactions, H-bonding, and stacking interactions among MON materials and dye molecules.[38]

Herein, we synthesized a Cu-based 2D MOF, i.e., 2D Cu-MOF, by using 4,4′-trimethylenedipyridine (TMDP) as an organic linker adopting a simple stirring method under ambient conditions. The synthesized 2D Cu-MOF was comprehensively characterized using a variety of spectroscopic techniques, and the crystal structure of the MOF was established using a single-crystal X-ray investigation. The top-down delamination of the synthesized 2D MOF was also carried out using the ultrasonication-induced liquid phase exfoliation (UILPE) approach to give the 2D Cu-MON layers. The morphological analysis was done to investigate the delamination after UILPE for different time duration as the duration of ultrasonication affects the extent of exfoliation into nanosheets. The application of these as-prepared 2D Cu-MONs after UILPE was assessed in the fields of drug delivery and wastewater treatment for the removal of various cationic and anionic dyes.

2. EXPERIMENTAL SECTION

2.1. Materials. All the chemicals were of analytical grade and procured from Sigma-Aldrich Chemical Co. (India) including 4,4′-trimethylenedipyridine (TMDP), copper(II) nitrate trihydrate [$Cu(NO_3)_2{\cdot}3H_2O$], methanol (MeOH), and acetonitrile (MeCN). The drug lansoprazole (LPZ) (≥98%) was also acquired from Sigma-Aldrich Chemical Co. (India). Aromatic dyes such as methylene blue (MB), methyl orange (MO), rhodamine B (RhB), and Congo red (CR) were also used. All the chemicals have been used without further purification.

2.2. Characterization. Fourier transform infrared (FTIR) spectral studies were done using PerkinElmer model GX spectrophotometer with KBr pellets in the 4000−400 cm^{-1} range. Electronic data were obtained using UV-3600 (Shimadzu) spectrophotometer. The PXRD patterns were recorded by the Miniflex II X-ray diffractometer with Cu Kα radiation (Shimadzu 6100).[23] TGA was recorded on a Shimadzu TGA-50H in the range 25−800 °C at a heating rate of 20 °C min^{-1} under a nitrogen atmosphere. The data for elemental analysis (C, H, and N) was gathered from the Central Drug Research Institute (CDRI) Micro-Analytical Laboratory in Lucknow, India. For morphological analysis, scanning electron microscopy (SEM) was done on JEOL JSM-6510LV, USA. Transmission electron microscopy (TEM) was performed with TECHNAI 200 kV (Fei, Electron Optics) fitted with 35 mm photography system and digital imaging, to

https://doi.org/10.1021/acsomega.2c08231
ACS Omega 2023, 8, 12232−12245

assess the morphology of synthesized material (organic and inorganic phases). The Brunauer–Emmett–Teller (BET) nitrogen isotherm analysis was carried out on Quantachrome ASiQwin at 77 K.

2.3. Synthesis of Cu-MOF. The Cu-MOF has been synthesized via slow evaporation technique according to the previously reported process.[39] For this reaction, 0.966 g of $Cu(NO_3)_2{\cdot}3H_2O$ with 0.396 g of TMDP were taken in a conical flask followed by the addition of a 20 mL of mixed solvent (MeOH/deionized, double distilled water (DDW), 1:1 ratio). Simultaneously, 20 μL of trimethylamine was poured into the above solution dropwise with continuous stirring. The whole reaction mixture was kept stirring on a magnetic stirrer under ambient conditions for 20 h (Scheme 1).

Scheme 1. Synthesis of 2D Cu-MON

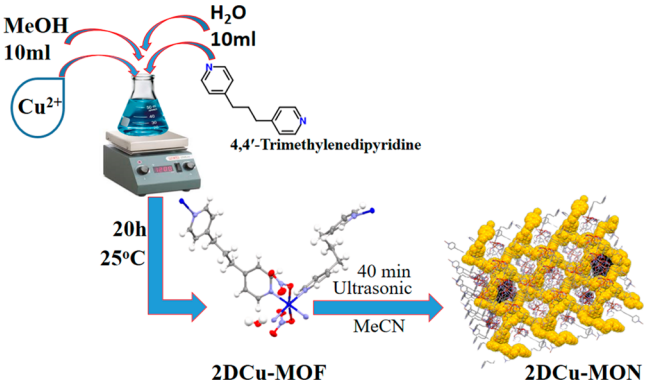

2.4. Single Crystal X-ray Diffraction (SCXRD) Studies. The crystal data of Cu-MOF was obtained at 100 K using graphite monochromated Mo Kα radiation on a Bruker-SMART APEX-CCD diffractometer (λ = 0.71073 Å).[40] From the International Tables for X-ray Crystallography, various parameters such as atomic scattering factors, anomalous dispersion corrections, and linear absorption coefficients were obtained, and data collection was performed via the APEX231 software,[41] whereas cell refinement and data reduction was performed with the SAINT software.[42] An empirical absorption correction has been applied for collected reflections through SADABS.[43] With anisotropic displacement parameters, all non-hydrogen atoms have been refined. Furthermore, parameters of the bond length were fixed by the use of several DIFX commands. Finally, the structures have been determined using Olex2, and solved with SIR-97 using direct approaches.[44] The CCDC reference number for 2D Cu-MOF is 2228511. A summary of the crystallographic data and the structure refinement for 2D Cu-MOF is provided in Table 1.

3. RESULTS AND DISCUSSION

3.1. Crystal Structure Description and Topology of 2D Cu-MOF. The SCXRD data were used to analyze the structure of Cu-MOF, i.e., $\{[Cu(TMDP)_2(NO_3)_2]{\cdot}H_2O\}_n$, which is a 2D Cu-MOF chain in which a metal–ligand system is generated by an intriguing bidentate mode of ligand binding. According to the X-ray diffraction data, $\{[Cu(TMDP)_2(NO_3)_2]{\cdot}H_2O\}_n$ crystallizes in the monoclinic system with $P2_1/n$ space group. The X-ray crystallographic data and refinement parameters are provided in Table 1, whereas selected bond lengths and angles are listed in Tables S1 and S2. The mononuclear unit of Cu-MOF contains one

Table 1. Crystallographic Data and Refinement Parameters for 2D Cu-MOF

empirical formula	$C_{52}H_{58}Cu_2N_{12}O_{13}$
formula weight	1186.20
temp (K)	100(2)
cryst syst	monoclinic
space group	$P2_1/n$
a (Å)	10.4987(8)
b (Å)	17.3344(13)
c (Å)	15.2266(12)
α (deg)	90
β (deg)	103.345(2)
γ (deg)	90
vol (Å^3)	2696.2(4)
Z	2
ρ_{calc} (g/cm^3)	1.4610
μ (mm^{-1})	0.864
$F(000)$	1233.9
cryst size (mm^3)	0.37 × 0.22 × 0.17
radiation	Mo Kα (λ = 0.71073)
2θ range for data collection (deg)	5.34 to 50.1
index ranges	$-13 \le h \le 13$, $-23 \le k \le 23$, $-20 \le l \le 20$
reflns collected	40981
indep reflns	4773 [R_{int} = 0.0786, R_{sigma} = 0.0495]
data/restraints/parameters	4773/0/364
goodness-of-fit on F^2	1.095
final R indexes [$I \ge 2\sigma(I)$]	R_1 = 0.0374, wR_2 = 0.0846
final R indexes [all data]	R_1 = 0.0525, wR_2 = 0.0957
largest diff. peak/hole (e Å^{-3})	0.42/−0.50

Cu(II) ion, two TMDP, and two NO_3 ligands, as shown in Figure 2a.

The central metal ion is surrounded by two oxygen atoms attached at the axial position, as well as four ligands of nitrogen located at the equatorial position, as depicted in Figure 2a. The TMDP ligand in this instance exhibits bidentate behavior and is cubic-shaped in the 2D Cu-MOF. Additionally, the Cu1–O1 distance is 2.4242(19) Å and the Cu–N distances are 2.018(2) Å for Cu1–N1 and 2.013(2) Å for Cu1–N3. Simultaneously, bond angles are O4–Cu1–O1 170.15°, N1–Cu1–O1 96.53°, N3–Cu1–O1 86.61°, and N3–Cu–O4 84.32°. In the 2D Cu-MOF, the H-bonding can occur intramolecularly or intermolecularly. Furthermore, the stability of the supramolecular network is greatly influenced by noncovalent interactions. However, the emergence of noncovalent contacts between the Cu-MOF neighboring moieties (i.e., O···H and $\pi\cdots\pi$) leads to the production of a 2D nanosheet, as shown in Figure 2(b–d).

The Cu(II) ion is surrounded by hexacoordinated bonds that give it the octahedral geometry as can be seen in the coordination polyhedron diagram (Figure 3). The linker produces helical chains through the self-assembly of Cu(II) ions, which results in a 2D network, according to a close study of the crystal packing analysis. Additionally, the layers undergo 2-fold interpenetration to yield tangled double layers, which appear as thick strands. So hydrogen bonds are what hold these strands together as they stack on top of one another as depicted in Figures 2 and 4. The layering arrangement in the MOF is interpenetrated (Figure 4a) and the topology of the 2D Cu-MOF was found to be *sql* as determined by TOPOS Pro program as shown in Figure 4b.

https://doi.org/10.1021/acsomega.2c08231
ACS Omega 2023, 8, 12232–12245

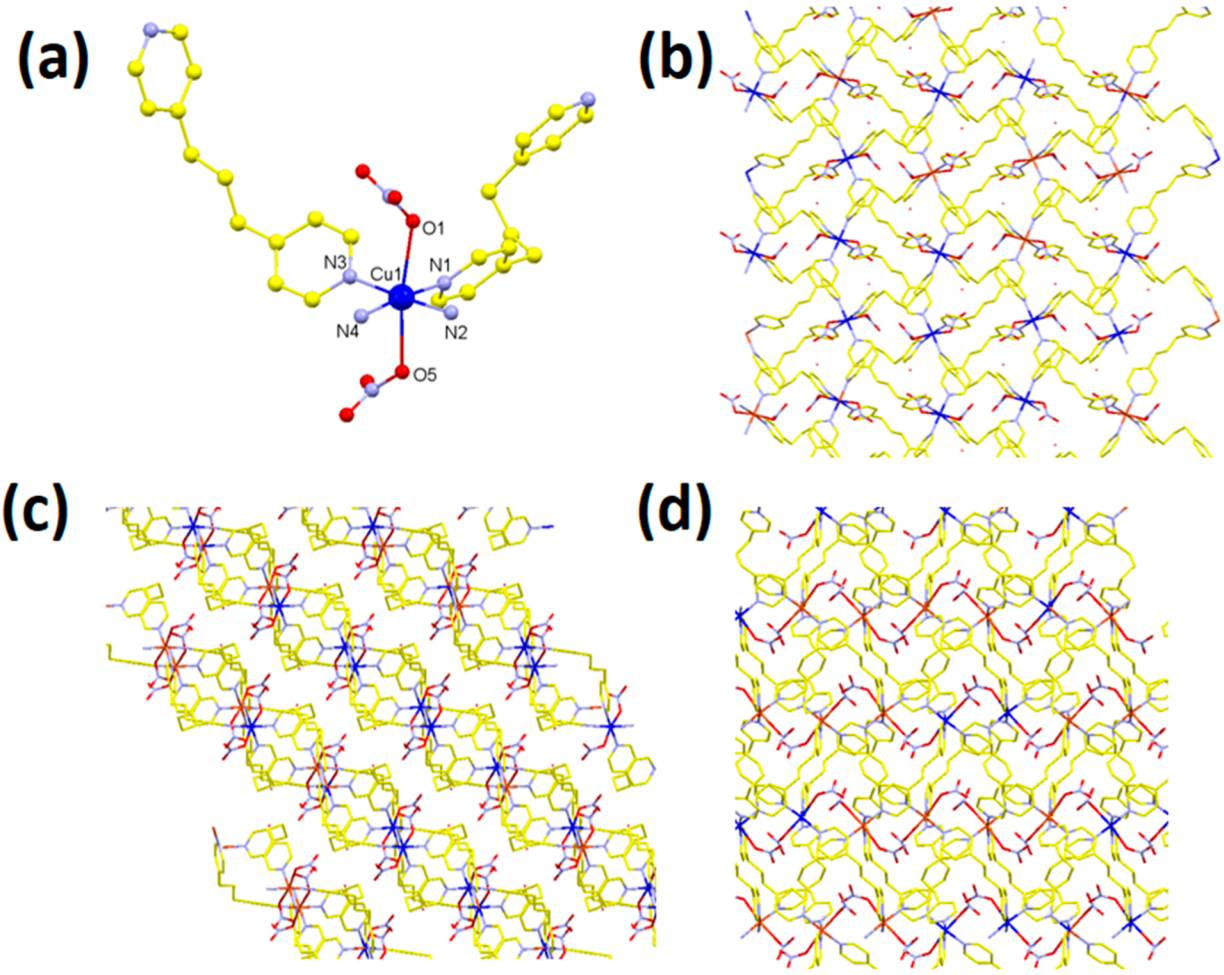

Figure 2. (a) Structure of the basic building block of 2D Cu-MOF, (b) intertwined double layer of 2D Cu-MOF, and (c, d) stacking of double layers of 2D Cu-MOF along *a* and *c* axes, respectively.

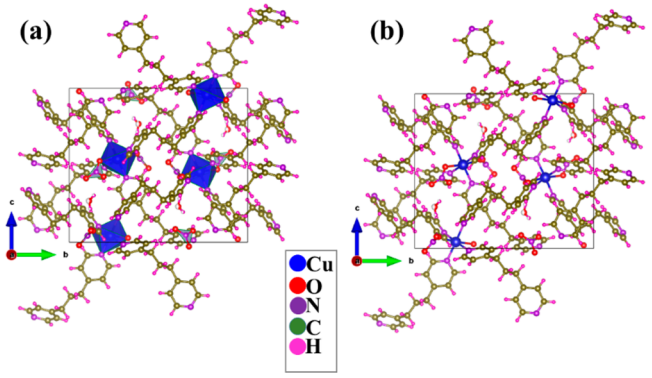

Figure 3. (a) Coordination polyhedron diagram of 2D Cu-MOF and (b) coordination environment around the metal ion in the packing diagram of 2D Cu-MOF.

The porosity of 2D Cu-MOF was assessed with the aid of N_2 adsorption isotherm, which demonstrated extremely low surface area as presented in Figure S1.

3.2. Top-Down Exfoliation of Bulk 2D Cu-MOF. As previously mentioned, tangled double layers of 2D Cu-MOF crowd on top of one another through hydrogen bonding. The crystals of bulk 2D Cu-MOF were ultrasonically treated in acetonitrile for different time duration to see if ultrasonication-induced liquid phase exfoliation (UILPE) could delaminate 2D

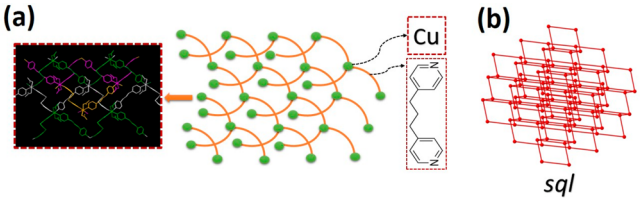

Figure 4. (a) Layering pattern in 2D Cu-MOF and (b) *sql* topology in the structure of 2D Cu-MOF.

tangled helical chains of the 2D Cu-MOF. The supernatant of the colloidal suspension of 2D Cu-MOF (Figure 5b) was tested via Tyndall light scattering effect.[45] It was found that Tyndall light scattering was best observed for the sample that was subjected to sonication for 40 min, implying that the bulk is well dispersed as few-layered 2D nanosheets in acetonitrile within a time duration of 40 min as shown in Figure 5d.

The morphological analysis of the obtained few-layered 2D Cu-MON was done using SEM and HR-TEM analysis. SEM analysis was used to assess the exfoliation of 2D Cu-MOF to 2D Cu-MON by drop-casting the supernatant of the colloidal suspension onto a silicon wafer. Surface morphology and lateral dimensions were examined by SEM analysis. The intertwined nature of the 2D Cu-MOF layers makes it challenging to exfoliate them as a single layer; instead multiples of at least two layers are anticipated to come off. Figure 6a–e

https://doi.org/10.1021/acsomega.2c08231
ACS Omega 2023, 8, 12232−12245

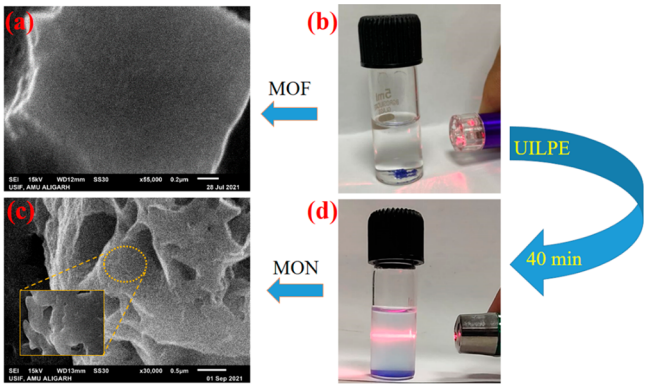

Figure 5. (a) SEM image of 2D Cu-MOF, (b) Tyndall light scattering observed for the acetonitrile suspension of 2D Cu-MOF before UILPE, (c) SEM image of 2D Cu-MON after UILPE, (d) Tyndall light scattering for the acetonitrile suspension of 2D Cu-MON after UILPE for 40 min.

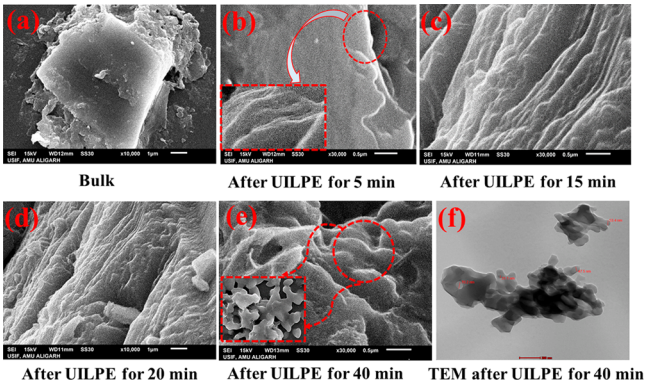

Figure 6. SEM images of 2D Cu-MOF (a) bulk and after UILPE for (b) 5 min, (c) 15 min, (d) 20 min, and (e) 40 min. (f) TEM micrograph of 2D Cu-MON after UILPE for 40 min.

demonstrates that upon increasing the time duration of UILPE, the exfoliation of nanosheets becomes more effective and visible as can be seen in the SEM micrograph upon UILPE for 40 min. The SEM micrograph (Figure 6e) clearly shows the delamination of 2D Cu-MOF into 2D nanosheets of micrometer lateral dimensions stacked on top of one another after exfoliation for 40 min.

TEM investigations were done to get better insights about the morphology and polymeric network assessment. The methanolic suspension of 2D Cu-MON was drop cast on a carbon-coated Cu-TEM grid, and it was observed that the sheets in the nanometer range of 30−55 nm are stacked on top of one another. This stacking of nanosheets can also be seen easily in the SEM micrograph (Figure 6f).

The SEM micrograph clearly demonstrates the top-down delamination of the bulk MOF into 2D nanosheets of micrometer lateral dimensions as shown in Figure 6a−e. A thorough examination of the crystal packing study reveals that the linker self-assembles into helical chains with the assistance of Cu(II) ions forming a 2D network. The layers are penetrated twice to produce intertwined double layers that look like thick strands. These threads lie on top of one another and are joined by hydrogen bonds as shown in Figure 7.

3.3. Drug Delivery and In Vitro Release Studies on 2D Cu-MON. The drug loading and release performance of 2D Cu-MON was investigated for the drug lansoprazole (LPZ).

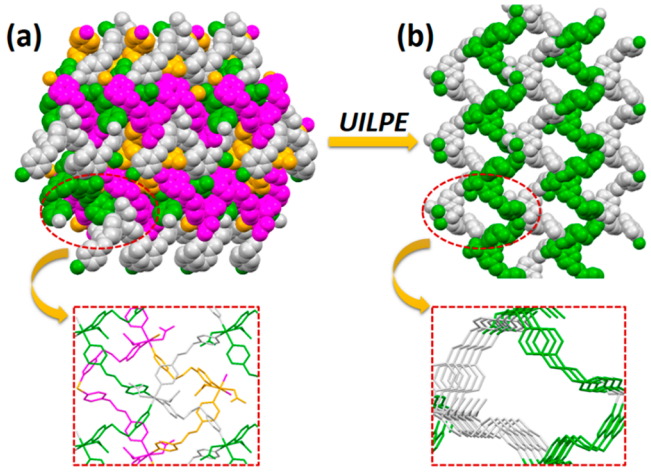

Figure 7. (a) Crystal packing diagram of 2D Cu-MOF down the *b* axis (various colors correspond to various layers) and (b) intertwined double layer (2D Cu-MON) of 2D Cu-MOF.

LPZ is usually employed for treating the signs of gastro-esophageal reflux disease (GERD), a condition in which the esophagus (the tube connecting the throat and stomach) might get injured due to the stomach acid flowing backward. Both adults and children with GERD experience heartburn and other symptoms of this condition.

For the drug loading experiment, 20 mg of 2D Cu-MON was dispersed in 10 mL of MeCN and treated through ultrasonication for 25 min. Then, 20 mg of LPZ dissolved in 10 mL of MeCN (2 mg/mL) was added to the former solution and ultrasonicated for further 15 min. Finally, the mixture of drug and 2D Cu-MON was stirred for 24 h under ambient conditions and the supernatant of the mixture was collected via centrifugation. The concentration of LPZ drug in the supernatant was determined by recording the UV−vis spectra before and after drug loading and finally the drug loading efficiency and content were calculated by using eqs 1 and 2:[46]

$$\text{loading efficiency (\%)} = \frac{\text{mass of loaded drug}}{\text{mass of drug loaded MONs}} \times 100 \quad (1)$$

$$\text{encapsulation efficiency (\%)} = \frac{\text{mass of loaded drug}}{\text{mass of total drug}} \times 100 \quad (2)$$

The UV−vis absorption spectra of the acetonitrile solution containing LPZ before and after drug loading on 2D Cu-MOF and 2D Cu-MON have been employed for evaluating the drug loading capacity as shown in Figure S2 and Figure 8, respectively. The characteristic LPZ absorption peak at 280 nm gets slightly diminished as can be seen in the absorption spectra of LPZ in MeCN solution after loading on 2D Cu-MOF (Figure S2) while it shows a marked decrease in the case of 2D Cu-MON as demonstrated in Figure 8a. Loading efficiency of 23.95% and 45.61% was observed for 2D Cu-MOF and 2D Cu-MON, respectively. The encapsulation efficiency was found to be around 31.50% and 83.51% for 2D Cu-MOF and 2D Cu-MON, respectively, as estimated from the standard concentration curve. The results indicated lower drug loading capacity of 2D Cu-MOF in comparison to 2D Cu-MON; hence, further drug release studies were performed on 2D Cu-MON.

https://doi.org/10.1021/acsomega.2c08231
ACS Omega 2023, 8, 12232−12245

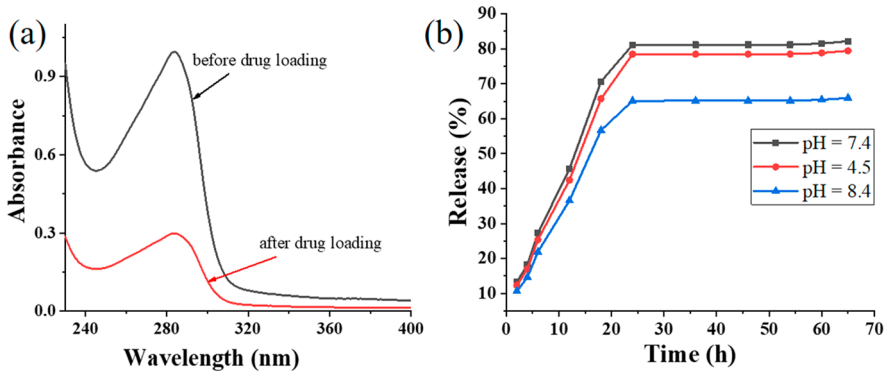

Figure 8. (a) UV−vis absorption spectra of the acetonitrile solution containing LPZ before and after LPZ loading on 2D Cu-MON. (b) In vitro LPZ nanosheet release profile at various pH values.

Table 2. Overview of Drug Encapsulation in MOFs

MOF/MON	metal ion	organic linker	inner pore size (Å)	drug	loading method	drug loading (%, w/w)	ref
MIL-101(Cr)	Cr	BDC	29−34	ibuprofen	impregnation	58	50
MIL-101(Fe)	Fe	BDC	29−34	ethoxysuccinatocisplatin prodrug	postsynthetic modification	12.8	51, 52
MIL-101(Cr)	Cr	BDC	29−34	ibuprofen	computational prediction	52.6	53
BioMIL-1	Fe	nicotinic acid		nicotinic acid	active molecules	71.5	54
NCP-1	Tb	disuccinato cisplatin		disuccinato cisplatin	active molecules	75	55
HKUST-1	Cu	BTC	6−12	5-FU	impregnation	33.3	56
Cu-BTC	Cu	BTC	9	5-FU	impregnation	45	57
2D Cu-MON	Cu	TMDP		lansoprazole	impregnation	83.5	this work

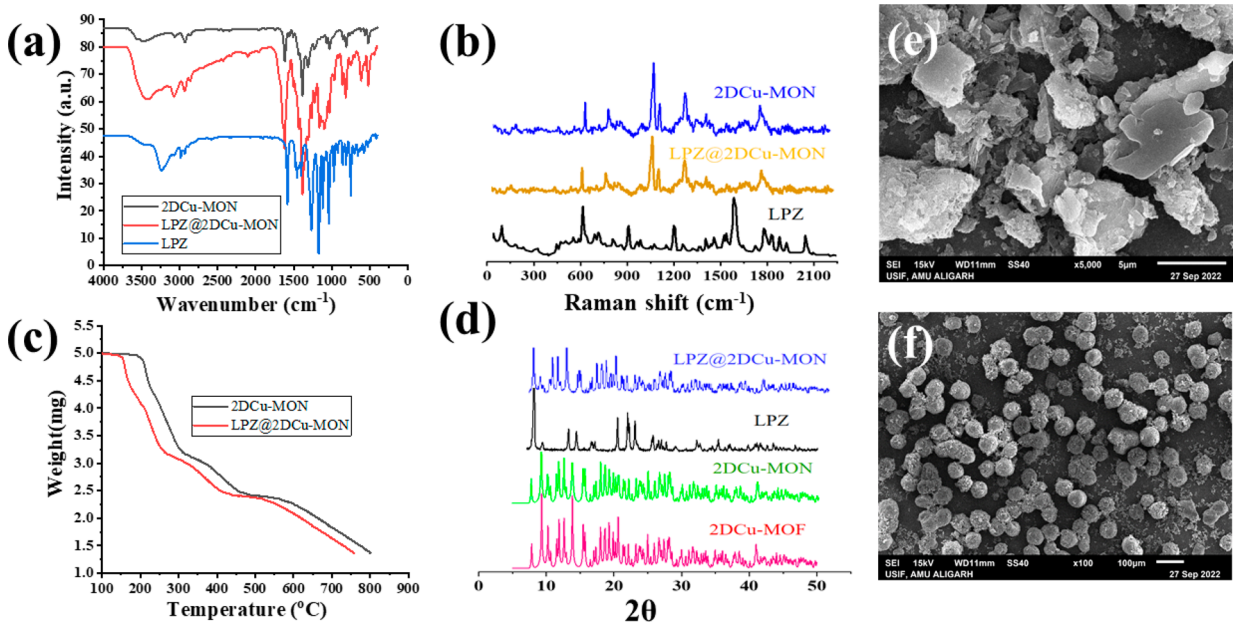

Figure 9. (a) FTIR spectra, (b) Raman spectra, (c) TGA plot, (d) PXRD patterns of LPZ, 2D Cu-MON, and LPZ@2D Cu-MON and (e, f) SEM micrograph of (e) 2D Cu-MON and (f) LPZ@2D Cu-MON.

The drug release profile is also an important parameter for drug formulations and for that purpose sustained drug release is a vital requirement. However, burst release is one of the main drawbacks that hampers the important application of drug delivery carriers in various viral infection and anticancer treatments. The *in vitro* drug release profile of LPZ@2D Cu-MON was examined under simulated physiological conditions at different pH conditions as explained below.

For the drug release studies, 20 mg of LPZ@2D Cu-MON was added into a 20 mL PBS buffer solutions (0.15 M) maintained at different pH values of 4.5, 7.4, and 8.4 in a conical flask and stirred at 37 °C via a magnetic stirrer. At various time intervals, a sample volume of 2 mL was collected

https://doi.org/10.1021/acsomega.2c08231
ACS Omega 2023, 8, 12232−12245

from the supernatant after centrifugation at 5000 rpm for 15 min and analyzed with the aid of UV−vis spectrophotometer. *In vitro* release analysis of LPZ@2D Cu-MON was carried out in three different pH media,[47] and the drug release (%) was calculated from eq 3:

$$\text{release (\%)} = \frac{\text{actual drug released at any time (mg)}}{\text{amount of drug loaded within MON (mg)}} \times 100 \quad (3)$$

It was observed that drug loaded 2D Cu-MON, i.e., LPZ@2D Cu-MON, exhibited slow drug release over a time period of 25 h with an almost linear profile over this period (Figure 8b). Furthermore, it can be seen that LPZ did not completely release and reached a plateau of 87.40%, 79.50%, and 64.81% at pH values of 7.4, 4.5, and 8.4, respectively. The above finding revealed that the drug release in acidic and neutral media was higher than that in the basic medium, which indicated that 2D Cu-MON is an excellent carrier for antiulcer drug delivery. The slow release of LPZ drug from the 2D Cu-MON suggested that most of the drug remains in the nanosheets which restricts the diffusion of drugs incorporated within them and suggested relative binding between LPZ molecules and the 2D Cu-MON. It was thus discovered that the drug release process is affected by the pH media and the type of material matrix.[48,49] Various MOFs and their drug delivery parameters are described in Table 2.[50−57]

3.3.1. Characterization of 2D Cu-MON and LPZ@2D Cu-MON. FTIR spectroscopy was used to assess the interaction between LPZ and 2D Cu-MON by analyzing the characteristic absorption peaks. The FTIR spectra of LPZ@2D Cu-MON was compared to that of pure LPZ and untreated 2D Cu-MON. The characteristic absorption peaks of LPZ appeared at 3245 and 2935 cm^{-1} corresponding to stretching vibration of −NH− and the intense peaks at 1600, 1375, and 1103 cm^{-1} belong to $-CH_2$, aromatic ring, and C−O and ether bond, respectively as shown in Figure 9a. In the case of 2D Cu-MON, the broad absorption peak at 3553 cm^{-1} corresponds to O−H υ of a water molecule present in the lattice. The peaks at 3075, 2938, and 2845 cm^{-1} depict the aromatic C═C−H υ and asymmetric and symmetric CH_2/CH_3 υ, respectively. The peak at 1622 cm^{-1} corresponds to the bending mode of H_2O molecule, a medium intensity peak at 1560 cm^{-1} corresponds to C−N υ of the bipyridyl ring, and a strong peak at 1386 cm^{-1} denotes the υ mode of nitrate group. The prominent peaks in the low frequency region 520−584 cm^{-1} depict the υ Cu−N vibrations. In the case of LPZ@2D Cu-MON spectrum, the lack of any shift in the LPZ and 2D Cu-MON characteristic peaks suggests that no new chemical bonds have been formed. Further, it was observed that there is a distinct match in the peaks of 2D Cu-MON before and after the drug loading. Consequently, this ruled out the possibility of an interaction between drug and 2D Cu-MON indicating that LPZ was dispersed on the nanosheets.[58,59]

Raman spectra of 2D Cu-MON containing LPZ or without LPZ have been recorded and compared to that of LPZ spectrum as presented in Figure 9b. The peaks corresponding to the 2D Cu-MON were well detected in LPZ@2D Cu-MON along with the peaks corresponding to LPZ presenting main peaks at 600, 900, 1200, and 1600 cm^{-1}. This is another technique that indicates the effective drug loading in the 2D Cu-MON. The peaks in the range of 1400−1600 cm^{-1} correspond to C−C cyclic ring stretching (benzimidazole and pyridine moieties) of LPZ as well as bipyridyl moiety of 2D Cu-MON. The peaks in the range of 1300−1250 cm^{-1} denote the C−N stretching bands of LPZ, whereas those at 600 and 900 cm^{-1} correspond to the in plane ring mode and symmetric ring breathing shifting and broadening. Overall, the Raman investigation confirmed the successful LPZ incorporation on the 2D Cu-MON without showing any shift in the characteristic peaks.

TGA has been performed in the range of 50−800 °C to examine the thermal stability of 2D Cu-MON before and after drug loading in a nitrogen atmosphere. The TGA pattern of 2D Cu-MON revealed the degradation via three step loss. The first slight weight loss of about 15% at 200 °C corresponds to the removal of water molecules that are present in the crystal lattice as shown in Figure 9c. In the second step, weight loss of ∼40% in the range of 232−335 °C corresponds to the degradation of ligand moiety. Finally, the remaining framework begins to deteriorate at temperature above 450 °C, and the final residue might be attributed to the presence of metal oxide. Moreover, the TGA patterns of the LPZ@2D Cu-MON also demonstrate three-step degradation but the former showed a loss at a temperature of 150 °C owing to the lesser thermal stability of the drug LPZ.

PXRD patterns of 2D Cu-MON, LPZ@2D Cu-MON, and pure LPZ have been investigated and are presented in Figure 9d. The PXRD pattern of exfoliated nanosheets matches well with that of bulk MOF with slight change in relative intensities owing to orientation effects. The phase purity of 2D Cu-MON was thus well established by comparing with the bulk material which confirms the retention of structural integrity after exfoliation. The PXRD pattern of LPZ displayed several characteristic peaks that depict the crystalline nature of the drug. However, the PXRD pattern showed no significant change after drug loading, i.e., in LPZ@2D Cu-MON, indicating that the drug has been loaded in an amorphous state which further facilitates drug release at target site with ease.[60] The surface morphology after drug loading was also assessed by recording the SEM micrographs. The SEM micrograph of 2D Cu-MON depicts the layered patterns of nanosheets randomly distributed as shown in Figure 9e. This enhanced surface area has been found to display remarkable drug loading on the surface of 2D Cu-MON. The SEM micrograph (Figure 9f) of drug loaded nanosheet, i.e., LPZ@2D Cu-MON, revealed the uniform distribution of globular shaped particles on the surface depicting the loading of drug.

3.4. Adsorption of Organic Dye Pollutants. Wastewater emerging from some chemical plants consists of organic dye pollutants. With a global dye usage of almost 700,000 tonnes, the textile industry emerged as one of the worst polluters.[61] Nearly all dyes are dangerous and carry a significant risk of causing malignant mutations; therefore, a variety of approaches have been employed in recent years to eliminate dye contaminants from wastewater.[62] The absorption method is one of them and is widely employed for the removal of aromatic dye molecules from wastewater since it is economical and easy to use.

To investigate the adsorption behavior of 2D Cu-MON for the removal of organic dyes such as MB, MO, RhB, and CR, an adsorption experiment was conducted by placing dye solution at 10 ppm concentration in a conical flask. To this dye solution (50 mL), 10 mg of the absorbent (2D Cu-MON) was added with continuous stirring. Aliquots of 2 mL were taken at different time intervals of 10, 20, 40, 60, 80, 100, and 120 min from the conical flask after centrifugation and assessed with the

https://doi.org/10.1021/acsomega.2c08231
ACS Omega 2023, 8, 12232−12245

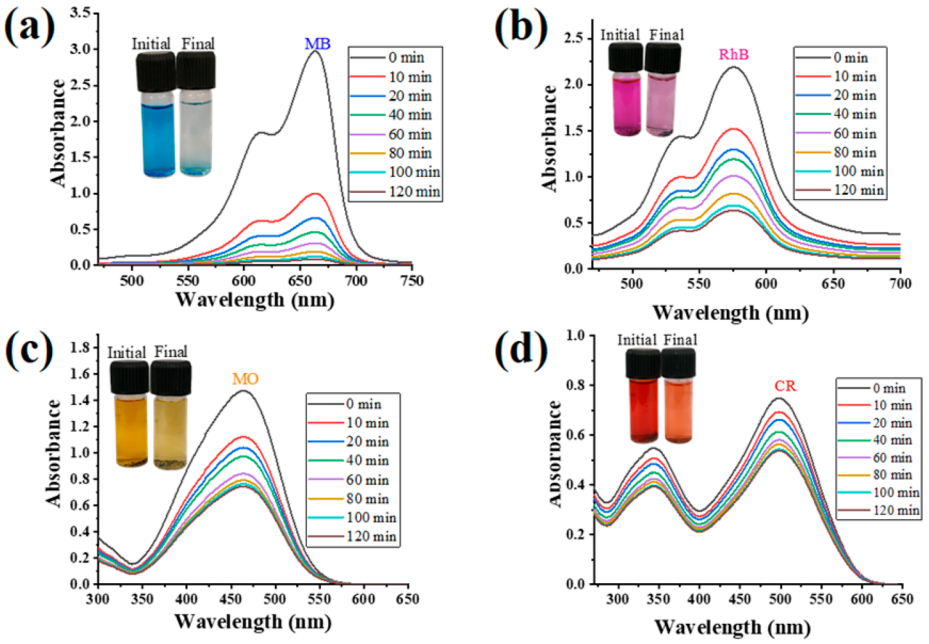

Figure 10. UV−vis spectra for adsorption of dyes including (a) MB, (b) RhB, (c) MO, and (d) CR by using 2D Cu-MON as an adsorbent.

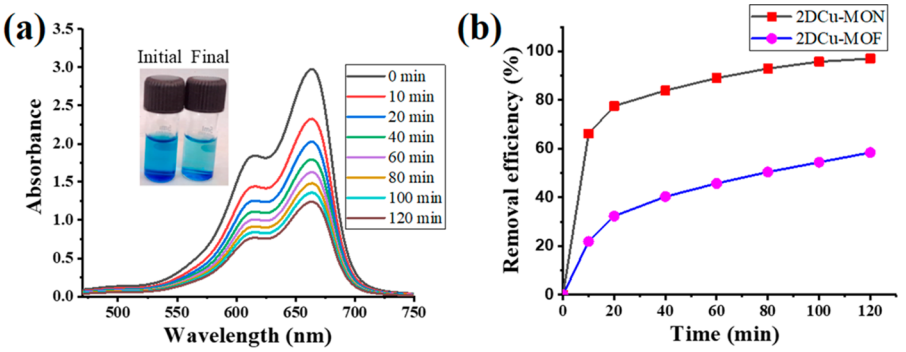

Figure 11. (a) UV−vis spectra for adsorption of MB dye by using 2D Cu-MOF as an adsorbent. (b) Comparison between removal efficiency of 2D Cu-MOF and 2D Cu-MON for MB dye.

aid of UV−vis spectrophotometer. In order to vary the pH of the solution, 0.1 M HCl and 0.1 N NaOH were also employed. The adsorption capacity and removal percentage of 2D Cu-MON toward different cationic and anionic dyes were calculated by using eqs 4 and 5:[63]

Adsorption capacity,

$$q_t = \frac{(C_0 - C_t)}{M} V \tag{4}$$

Removal efficiency,

$$R\ (\%) = \frac{(C_0 - C_t)}{C_0} \times 100 \tag{5}$$

where C_0 (ppm) is the initial dye concentration, C_t (ppm) indicates the dye concentration after adsorption at different time intervals (t), V represents the volume of the dye solution, and M is the mass of the 2D Cu-MON (absorbent) in milligrams.

In this work, four distinct aromatic dyes with various size and charge including cationic dyes (MB and RhB) and anionic dyes (MO and CR) were used to evaluate the dye adsorption behavior of 2D Cu-MON as shown in Figure 10. The absorption spectra (Figure 10) revealed that 2D Cu-MON has excellent adsorption capability for cationic dyes such as MB and RhB. The absorption maxima of MB and RhB dye observed at 664 and 463 nm, respectively, were lowered within 10 min with 66.1% and 42.5% adsorption efficiencies. The absorption peak largely vanished after 120 min for MB dye and reached 97.12% efficiency (Figure 10a) while 80.5% efficiency was reached for RhB (Figure 10b) by utilizing 2D Cu-MON as an absorbent. The absorption maximum at 464 nm of the MO dye diminished slightly and displayed a removal percentage of 49.7% (Figure 10c), whereas CR (absorption maxima at 498 nm) only had a removal efficiency of 30.55% within 160 min (Figure 10d), which is a significantly lower proportion as compared to the cationic dyes. with the assistance of eq 4, the adsorption capacity of 2D Cu-MON (adsorbent) for MB and RhB was found to be 61.72 mg/g and 59.55 mg/g, respectively. The maximum removal of cationic MB dye could be attributed to the electrostatic cation−π interactions between the cationic part of the dye and π electron cloud of the aromatic ring present in 2D Cu-MON. However, another reason behind effective and speedy adsorption of MB dye is the smaller size and linear structure of the MB molecule. On the other hand, RhB also being a cationic dye showed lower removal owing to

https://doi.org/10.1021/acsomega.2c08231
ACS Omega 2023, 8, 12232−12245

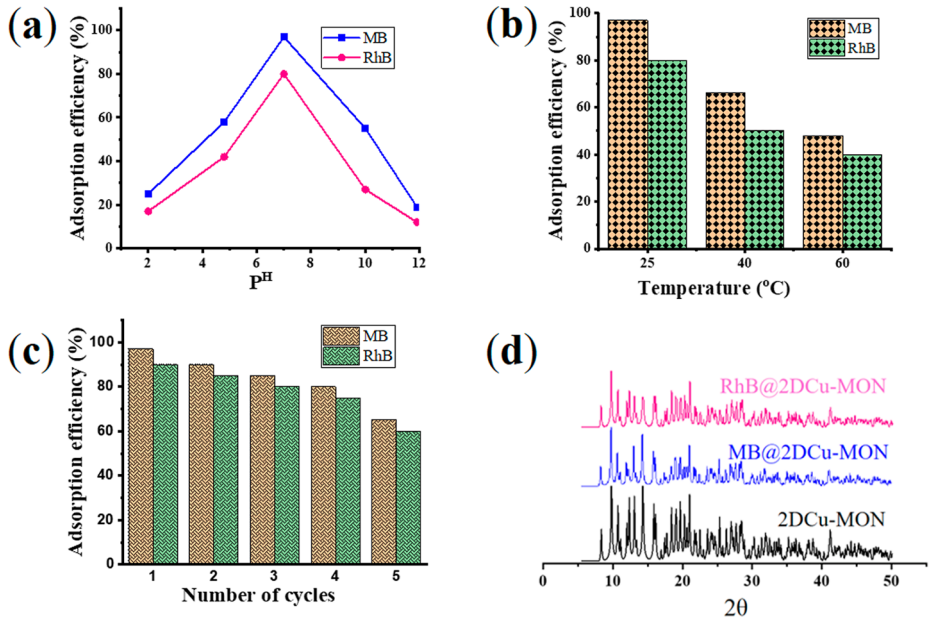

Figure 12. (a) Influence of pH, (b) effect of temperature on dye (MB and RhB) adsorption, (c) recyclability of adsorbent 2D Cu-MON, and (d) PXRD pattern of 2D Cu-MON before and after adsorption of MB and RhB dye.

its nonlinear structure and larger size that imparts hindrance in its adsorption on the surface of 2D Cu-MON adsorbent.

Dye adsorption capability for the removal of cationic dye MB was also assessed by using 2D Cu-MOF as an adsorbent, and it was observed that removal efficiency of ∼46% was achieved in 120 min in comparison to about 97% in case of 2D Cu-MON (Figure 11). The enhanced dye removal in the case of 2D Cu-MON could be attributed to the exfoliation in the form of few-layered nanosheets that provide more surface area for the adsorption of dye molecules.

3.4.1. Selectivity for Organic Dyes. The achievement of selective adsorption for particular dye contaminants is quite relevant as well as difficult for an environmental scientist. It was observed that the cationic dyes (MB and RhB) were quickly absorbed by the 2D Cu-MON; hence, it was also investigated whether the framework could help with selective adsorption of the dye. Therefore, to assess the selectivity for organic dyes, a thorough experiment was conducted by introducing two different dyes to form a solution mixture, and the adsorption process was studied using a UV−vis spectrophotometer. It has been observed that 2D Cu-MON adsorbs dye from a solution mixture in a selective manner.

It is noteworthy to mention that 2D Cu-MON successfully adsorb cationic dyes, i.e., MB and RhB, in the presence of the anionic dyes (MO and CR) as shown in Figure S3a−d. Additionally, the selectivity of cationic dyes in a mixture of all the four dyes, viz., MB, RhB, MO, and CR, was also observed with the removal efficiency of about 82.6% and 28.1% for MB and RhB, respectively, comparatively higher than the anionic dyes with 9.1% (MO) and 10% (CR) removal efficiency as demonstrated in Figure S3e. It can thus be concluded from these results that 2D Cu-MON could quickly and selectively adsorb cationic dyes from a mixture of cationic and anionic dye solutions.

3.4.2. Effect of pH. The pH of reaction is a critical component to such adsorption events from an application standpoint. The surface charge, dye structure, and level of ionization of dye components are all greatly influenced by the pH. As shown in Figure S4, the PXRD patterns under diverse pH conditions ranging from 2 to 12 have been investigated indicating that the 2D Cu-MON is quite stable at different pH values.

In order to assess the effect of pH on the adsorption phenomena on the surface of 2D Cu-MON, the cationic dyes with maximum removal percentage, i.e., MB and RhB, were utilized. Diverse sets of adsorption experiments were conducted by varying the pH in the range of 2−12 to explore the impact of pH by using 0.1 M HCl and 0.1 N NaOH solution. It can be concluded from Figure 12a that 2D Cu-MON adsorption efficiency increases when the pH of both dye solutions rises from 2 to 7. The reason behind this behavior could be that the adsorbent surface becomes protonated at low pH values resulting in H^+ ions competing with the cationic moiety of the dye and thus reducing adsorption efficacy. The maximum removal efficiency for both cationic dyes (MB and RhB) was observed at neutral pH (7). For both the dyes, the removal efficiency was found to be lower under harsh conditions, i.e., highly acidic or alkaline conditions, and appreciable reduction in adsorption behavior was observed. This reduction could be attributed to some structural changes in the adsorbent (2D Cu-MON) or due to the interference from the ionic species in the surrounding environment. These findings imply that 2D Cu-MON as an adsorbent has a remarkable capacity for cationic dye adsorption at pH = 7.

3.4.3. Effect of Temperature. Temperature is another physicochemical parameter which has a major influence on the adsorption capacity of 2D Cu-MON (adsorbent). The removal efficiency of 2D Cu-MON for MB and RhB dye adsorption was assessed in the temperature range between 25 and 60 °C (Figure 12b). Generally, an endothermic process is involved when adsorption efficiency increases with an increase in temperature, while decrease in adsorption efficiency with temperature rise indicates an exothermic process. The adsorption effectiveness of 2D Cu-MON for MB dye was found to be maximum at room temperature (25 °C) and rapidly decreased as the temperature further increased from 40

https://doi.org/10.1021/acsomega.2c08231
ACS Omega 2023, 8, 12232−12245

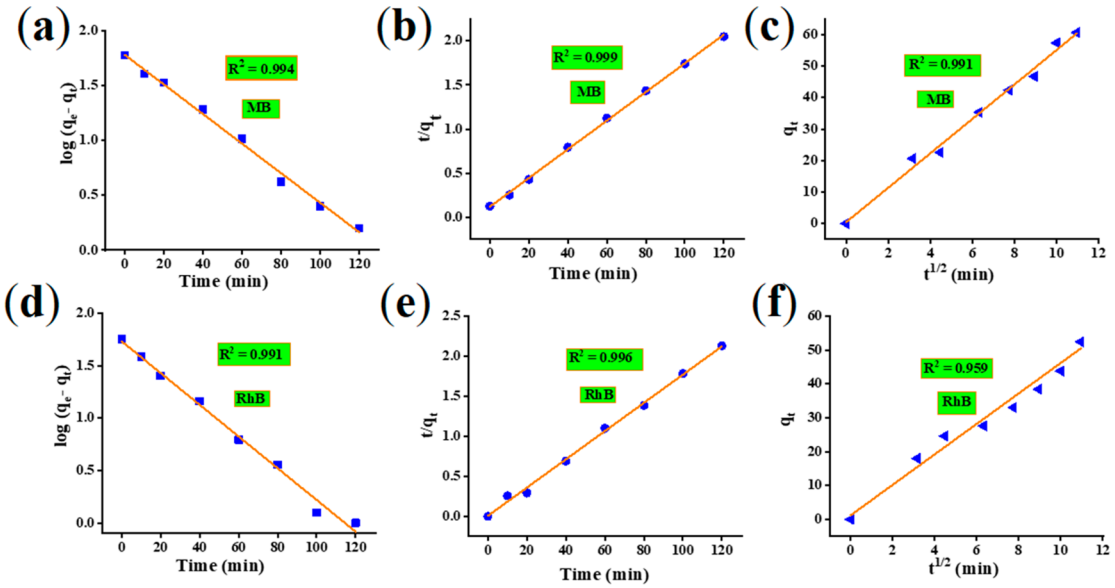

Figure 13. Adsorption kinetic plots of MB and RhB dye onto 2D Cu-MON using (a, d) pseudo-first-order, (b, e) pseudo-second-order, and (c, f) intraparticle kinetics models.

to 60 °C. This decrease in adsorption efficiency when the temperature is further raised indicates that the adsorption phenomenon follows an exothermic reaction.[64]

3.4.4. Reusability Study. Recyclability of the as-synthesized adsorbent is a critical component of wastewater treatment from an application standpoint. Following the dye adsorption process, the 2D Cu-MON adsorbent was repeatedly rinsed with ethanol solvent until all dye molecules were eliminated; after that the adsorbent was reused for the next adsorption cycle. As demonstrated in Figure 12c, the adsorbent was functional up to four cycles with an impressive adsorption efficiency for MB. Furthermore, efficiency starts to decline after the fourth cycle and showed lower efficiency in the fifth cycle, which occurs as a result of decrease in the number of open sites for adsorption. After the fourth adsorption cycle, the PXRD pattern was evaluated for MB adsorbed 2D Cu-MON (MB@2D Cu-MON) as well as RhB@2D Cu-MON showing that the framework was unaltered throughout the adsorption/desorption procedure as shown in Figure 12d.

3.4.5. Adsorption Kinetics. UV−vis spectra revealed maximum adsorption of cationic dyes on the surface of 2D Cu-MON as compared to the anionic dyes. Moreover, the adsorption behavior was evaluated at different time intervals, and finally the reaction adsorption kinetics was investigated. In order to comprehend the kinetics of the adsorption process, three adsorption kinetic models were employed including pseudo-first-order, pseudo-second-order, and intraparticle diffusion.[65] The calculated kinetic parameters are provided in Table S3.

The pseudo-first-order rate is given by eq 6 as follows:

$$\log(q_e - q_t) = \log q_e - \frac{k_1}{2.303}t \tag{6}$$

where q_e and q_t (mg/g) indicate the dye adsorption capacity at equilibrium and at time t and k_1 (min^{-1}) is the pseudo-first-order rate constant. Using the pseudo-first-order rate equation, the slope of the $\log(q_e - q_t)$ vs time plot was used to compute all kinetic parameters. The rate constant is roughly consistent with past literature findings, but the R^2 (correlation coefficient) value did not line up with the graph. Due to discrepancies between the calculated and experimental adsorption capacity values, this model cannot be applied to explain the adsorption phenomenon.

The pseudo-second-order rate is given by eq 7 as follows:

$$\frac{t}{q_t} = \frac{1}{k_2 q_e^{\,2}} + \frac{t}{q_e} \tag{7}$$

Here, q_e and q_t (mg/g) indicate the dye adsorption capacity at equilibrium and at time t and k_2 (g/(mg min)) is the rate constant of pseudo-second-order, and it is determined by plotting t/q_t against time. The pseudo-second-order pattern shows good linearity and the R^2 value is close to 1 as demonstrated in Figure 13, as estimated and experimental q_e values are also quite similar. The adsorption of contaminants like dyes can thus be demonstrated using this model.

Intraparticle diffusion is given by eq 8 as follows:

$$q_t = K_3 t^{1/2} \tag{8}$$

In this case, q_t (mg/g) is the adsorption capacity of dye at time t and K_3 (mg/(g $min^{1/2}$)) is the rate constant of intraparticle diffusion. This model is also not appropriate for adsorption kinetics as shown by the conflicting values of estimated and experimental adsorption capacity values.

3.4.6. Adsorption Mechanism. The essential factors affecting dye adsorption capacity from wastewater are the surface properties of the material framework and the functional and structural behavior of the dye molecules. Ion exchange, hydrogen bonds, acid−base interactions, electrostatic interactions, and $\pi-\pi$ interactions are among the many processes that control adsorption as has already been documented in previous studies.[66] In the present work, the plausible adsorption mechanism could be explained on the basis of electrostatic cation−π and $\pi-\pi$ interactions that are responsible for the quick adsorption of cationic dye to the surface of 2D Cu-MON as depicted in Figure 14. The primary reason for enhanced MB and RhB dye adsorption could be attributed to the cationic nature of both the dyes that interact electrostatically with the nucleophilic aromatic ring of the

https://doi.org/10.1021/acsomega.2c08231
ACS Omega 2023, 8, 12232−12245

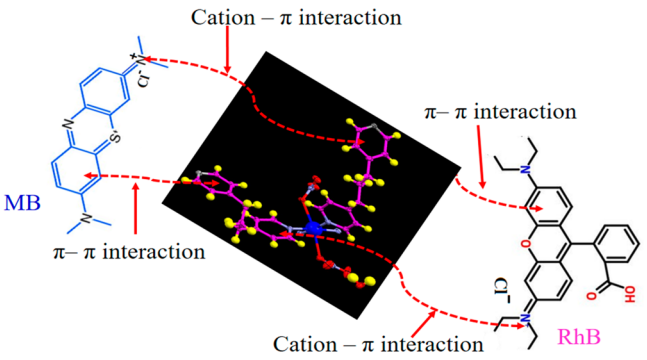

Figure 14. Plausible mechanism for the adsorption of MB and RhB dye by using 2D Cu-MON as an adsorbent.

TMDP ligand present in 2D Cu-MON. Moreover, the most efficient and highest adsorption of MB dye could not be only attributed to the cationic nature of dye but also to the linear structure of MB dye facilitating the ease in the adsorption of MB molecules over the sites available on the adsorbent.[67] Another cationic dye, RhB, shows good adsorption efficiency after MB for its adsorption on the 2D Cu-MON. The reason for the decline in the adsorption of RhB could be attributed to its nonlinear structure and bulkiness, which ultimately pose a hindrance for swift approach of it toward the framework, and thus it exhibits lower adsorption than MB.

On the other hand, the electrostatic repulsion between the nucleophilic aromatic ring of TMDP ligand in 2D Cu-MON and the anionic dyes (MO and CR) resulted in insignificant adsorption capacities compared to the cationic dyes.[68,69] In addition, the adsorption mechanism involved and the adsorption capacities for the removal of various organic pollutants by several 2D MOFs reported earlier are given in Table 3. The mechanism of adsorption by 2D Cu-MON was compared to these reported 2D MOFs depicting the involvement of similar types of mechanism patterns, viz., electrostatic interactions and $\pi-\pi$ interactions.

4. CONCLUSION

This work reports the facile synthesis of 2D Cu-MOF via a simple stirring method followed by slow evaporation under ambient conditions. The single crystal X-ray structure determination revealed that the reaction of TMDP with $Cu(NO_3)_2{\cdot}3H_2O$ resulted in a multilayered MOF which could further be delaminated to form 2D Cu-MONs by UILPE, as supported by Tyndall light scattering and other morphological analysis. The sonication process helped to improve the surface area which ultimately proved beneficial toward LPZ drug loading efficiency by 2D Cu-MON. The drug release in acidic medium was higher than that in basic medium indicating that 2D Cu-MON is an excellent carrier for antiulcer drug delivery. In addition, the developed 2D Cu-MON can also be effectively employed as an efficient adsorbent for removing cationic MB dye with 97% removal efficiency from wastewater. Simultaneously, the 2D Cu-MON can be employed to selectively adsorb the cationic dye even in the presence of anionic dye. The adsorption kinetics data revealed pseudo-second-order kinetics which shows a better agreement with the adsorption process. It was also suggested that cation$-\pi$, electrostatic, and $\pi-\pi$ interactions influence the fast adsorption of cationic dyes onto the surface of the 2D Cu-MON with recyclability for up to five cycles. This finding gives a new dimension to the application of 2D MONs in the fields of drug delivery and environmental remediation.

■ ASSOCIATED CONTENT

Supporting Information

The Supporting Information is available free of charge at https://pubs.acs.org/doi/10.1021/acsomega.2c08231.

Crystallographic information file for 2D Cu-MOF (CIF)

Bond lengths and bond angles of 2D Cu-MOF, different kinetic model parameters for adsorption of MB and RhB, BET isotherm (at 77 K) for 2D Cu-MOF, UV–vis spectra before and after LPZ loading on 2D Cu-MOF, PXRD patterns of 2D Cu-MON at different pH values, and UV–vis spectra for the determination of selectivity among dyes using 2D Cu-MON as an adsorbent (PDF)

■ AUTHOR INFORMATION

Corresponding Author

M. Shahid − *Functional Inorganic Materials Lab (FIML), Department of Chemistry, Aligarh Muslim University, Aligarh 202002, India*; orcid.org/0000-0003-3817-0286; Email: shahid81chem@gmail.com

Authors

Khalil M. A. Qasem − *Functional Inorganic Materials Lab (FIML), Department of Chemistry, Aligarh Muslim University, Aligarh 202002, India*

Table 3. Summary of the Performance of Adsorption Capacities of a Few 2D MOFs for Organic Pollutants at Room Temperature

materials	mechanism	Q_0, (mg/g)	adsorption kinetics model	ref
2D BUC-17	electrostatic interaction, ion exchange, hydrogen bonding, $\pi-\pi$ interaction	CR	pseudo-second-order	70
Fe-MIL-101	electrostatic interaction, ion exchange, hydrogen bonding, $\pi-\pi$ interaction	MO > MB	pseudo-second-order	71
Cu(II)−$5N_3$IP	hydrogen-bonding, $\pi-\pi$ interaction	MB > CR > RhB > MO	pseudo-second-order	72
2D Cu and Co based MOF	electrostatic interaction, $\pi-\pi$ interaction, H-bonding	MB > MO	pseudo-second-order	73
2D Zn-based MOF	electrostatic interaction, $\pi-\pi$ interaction	MB > MO	pseudo-second-order	74
Zn(II)/Cd(II) Based MOF	electrostatic interaction, $\pi-\pi$ interaction	MV > MB > MO > RhB	pseudo-second-order	75
2D Ni-based MOF	electrostatic interaction, $\pi-\pi$ interaction	MB > MO	pseudo-second-order	76
2D Cu-MOF	electrostatic interaction, $\pi-\pi$ interaction	MB > Rh−B > MO > CR	pseudo-second-order	this work

https://doi.org/10.1021/acsomega.2c08231
ACS Omega 2023, 8, 12232−12245

Shabnam Khan − *Functional Inorganic Materials Lab (FIML), Department of Chemistry, Aligarh Muslim University, Aligarh 202002, India;* orcid.org/0000-0003-1408-2628

Hatem A. M. Saleh − *Functional Inorganic Materials Lab (FIML), Department of Chemistry, Aligarh Muslim University, Aligarh 202002, India*

Younes S. A. Ghanem − *Functional Inorganic Materials Lab (FIML), Department of Chemistry, Aligarh Muslim University, Aligarh 202002, India*

Mohsen T. A. Qashqoosh − *Functional Inorganic Materials Lab (FIML), Department of Chemistry, Aligarh Muslim University, Aligarh 202002, India*

Musheer Ahmad − *Department of Applied Chemistry (ZHCET), Aligarh Muslim University, Aligarh 202002, India;* orcid.org/0000-0002-7446-0232

Complete contact information is available at: https://pubs.acs.org/10.1021/acsomega.2c08231

Author Contributions

[▽]K.M.A.Q. and S.K. contributed equally.

Notes

The authors declare no competing financial interest.

■ ACKNOWLEDGMENTS

The authors are thankful to the Chairperson, DST-FIST and DRS-SAP(II), Department of Chemistry, Aligarh Muslim University, Aligarh, for providing necessary research facilities. S.K. is grateful for the financial assistance from CSIR, New Delhi, for the Research Associateship [09/112(0665)/2020-EMR-I]. The authors also wish to thank SAIF-AIIMS for TEM analysis.

■ REFERENCES

(1) Novoselov, K. S.; Geim, A. K.; Morozov, S. V.; Jiang, D.; Zhang, Y.; Dubonos, S. V.; Grigorieva, I. V.; Firsov, A. A. Electric Field Effect in Atomically Thin Carbon Films. *Science (80-.).* **2004**, *306* (5696), 666−669.

(2) Geim, A. K.; Novoselov, K. S. The Rise of Graphene. *Nat. Mater.* **2007**, *6* (3), 183−191.

(3) Dreyer, D. R.; Todd, A. D.; Bielawski, C. W. Harnessing the Chemistry of Graphene Oxide. *Chem. Soc. Rev.* **2014**, *43* (15), 5288−5301.

(4) Pakdel, A.; Bando, Y.; Golberg, D. Nano Boron Nitride Flatland. *Chem. Soc. Rev.* **2014**, *43* (3), 934−959.

(5) Wang, H.; Li, C.; Fang, P.; Zhang, Z.; Zhang, J. Z. Synthesis, Properties, and Optoelectronic Applications of Two-Dimensional MoS 2 and MoS 2-Based Heterostructures. *Chem. Soc. Rev.* **2018**, *47* (16), 6101−6127.

(6) Liu, J.; Wang, H.; Antonietti, M. Graphitic Carbon Nitride "Reloaded": Emerging Applications beyond (Photo) Catalysis. *Chem. Soc. Rev.* **2016**, *45* (8), 2308−2326.

(7) Yang, L.-M.; Dornfeld, M.; Frauenheim, T.; Ganz, E. Glitter in a 2D Monolayer. *Phys. Chem. Chem. Phys.* **2015**, *17* (39), 26036−26042.

(8) Tan, Z.; Chen, S.; Peng, X.; Zhang, L.; Gao, C. Polyamide Membranes with Nanoscale Turing Structures for Water Purification. *Science (80-.).* **2018**, *360* (6388), 518−521.

(9) Colson, J. W.; Woll, A. R.; Mukherjee, A.; Levendorf, M. P.; Spitler, E. L.; Shields, V. B.; Spencer, M. G.; Park, J.; Dichtel, W. R. Oriented 2D Covalent Organic Framework Thin Films on Single-Layer Graphene. *Science (80-.).* **2011**, *332* (6026), 228−231.

(10) (a) Ye, W.; Yang, Y.; Fang, X.; Arif, M.; Chen, X.; Yan, D. 2D Cocrystallized Metal-Organic Nanosheet Array as an Efficient and Stable Bifunctional Electrocatalyst for Overall Water Splitting. *ACS Sustain. Chem. Eng.* **2019**, *7* (21), 18085−18092. (b) Ran, J.; Qu, J.; Zhang, H.; Wen, T.; Wang, H.; Chen, S.; Song, L.; Zhang, X.; Jing, L.; Zheng, R.; Qiao, S.-Z. 2D Metal Organic Framework Nanosheet: A Universal Platform Promoting Highly Efficient Visible-light-induced Hydrogen Production. *Adv. Energy Mater.* **2019**, *9* (11), 1803402. (c) Moghzi, F.; Soleimannejad, J.; Sañudo, E. C.; Janczak, J. Dopamine Sensing Based on Ultrathin Fluorescent Metal-Organic Nanosheets. *ACS Appl. Mater. Interfaces* **2020**, *12* (40), 44499−44507. (d) Pang, W.; Shao, B.; Tan, X.-Q.; Tang, C.; Zhang, Z.; Huang, J. Exfoliation of Metal-Organic Frameworks into Efficient Single-Layer Metal-Organic Nanosheet Electrocatalysts by the Synergistic Action of Host-Guest Interactions and Sonication. *Nanoscale* **2020**, *12* (6), 3623−3629. (e) Maka, V. K.; Mukhopadhyay, A.; Savitha, G.; Moorthy, J. N. Fluorescent 2D Metal-Organic Framework Nanosheets (MONs): Design, Synthesis and Sensing of Explosive Nitroaromatic Compounds (NACs). *Nanoscale* **2018**, *10* (47), 22389−22399. (f) Zhang, X.; Zhang, P.; Chen, C.; Zhang, J.; Yang, G.; Zheng, L.; Zhang, J.; Han, B. Fabrication of 2D Metal-Organic Framework Nanosheets with Tailorable Thickness Using Bio-Based Surfactants and Their Application in Catalysis. *Green Chem.* **2019**, *21* (1), 54−58.

(11) (a) Wang, X.; Chi, C.; Zhang, K.; Qian, Y.; Gupta, K. M.; Kang, Z.; Jiang, J.; Zhao, D. Reversed Thermo-Switchable Molecular Sieving Membranes Composed of Two-Dimensional Metal-Organic Nanosheets for Gas Separation. *Nat. Commun.* **2017**, *8* (1), 14460. (b) Rodenas, T.; Luz, I.; Prieto, G.; Seoane, B.; Miro, H.; Corma, A.; Kapteijn, F.; i Xamena, F. X. L.; Gascon, J. Metal-Organic Framework Nanosheets in Polymer Composite Materials for Gas Separation. *Nat. Mater.* **2015**, *14* (1), 48−55.

(12) Han, B.; Ou, X.; Deng, Z.; Song, Y.; Tian, C.; Deng, H.; Xu, Y.; Lin, Z. Nickel Metal-Organic Framework Monolayers for Photoreduction of Diluted CO2: Metal-node-dependent Activity and Selectivity. *Angew. Chemie Int. Ed.* **2018**, *57* (51), 16811−16815.

(13) Liu, J.-H.; Yang, L.-M.; Ganz, E. Electrochemical Reduction of CO 2 by Single Atom Catalyst TM-TCNQ Monolayers. *J. Mater. Chem. A* **2019**, *7* (8), 3805−3814.

(14) Liu, J.-H.; Yang, L.-M.; Ganz, E. Efficient and Selective Electroreduction of CO2 by Single-Atom Catalyst Two-Dimensional TM-Pc Monolayers. *ACS Sustain. Chem. Eng.* **2018**, *6* (11), 15494−15502.

(15) Campbell, M. G.; Liu, S. F.; Swager, T. M.; Dinca, M. Chemiresistive Sensor Arrays from Conductive 2D Metal-Organic Frameworks. *J. Am. Chem. Soc.* **2015**, *137* (43), 13780−13783.

(16) Bello, M. G.; Yang, Y.; Wang, C.; Wu, L.; Zhou, P.; Ding, H.; Ge, X.; Guo, T.; Wei, L.; Zhang, J. Facile Synthesis and Size Control of 2D Cyclodextrin-Based Metal-Organic Frameworks Nanosheet for Topical Drug Delivery. *Part. Part. Syst. Charact.* **2020**, *37* (11), 2000147.

(17) Gao, X.; Cui, R.; Zhang, M.; Liu, Z. Metal-Organic Framework Nanosheets That Exhibit PH-Controlled Drug Release. *Mater. Lett.* **2017**, *197*, 217−220.

(18) Liu, L.-L.; Chen, J.; Zhang, Y.; Yu, C.-X.; Du, W.; Sun, X.-Q.; Zhang, J.-L.; Hu, F.-L.; Mi, Y.; Ma, L.-F. Fabrication of Ultrathin Single-Layer 2D Metal-Organic Framework Nanosheets with Excellent Adsorption Performance via a Facile Exfoliation Approach. *J. Mater. Chem. A* **2021**, *9* (1), 546−555.

(19) Ashworth, D. J.; Foster, J. A. Metal-Organic Framework Nanosheets (MONs): A New Dimension in Materials Chemistry. *J. Mater. Chem. A* **2018**, *6* (34), 16292−16307.

(20) Coleman, J. N.; Lotya, M.; O'Neill, A.; Bergin, S. D.; King, P. J.; Khan, U.; Young, K.; Gaucher, A.; De, S.; Smith, R. J.; Shvets, I. V.; Arora, S. K.; Stanton, G.; Kim, H. Y.; Lee, K.; Kim, G. T.; Duesberg, G. S.; Hallam, T.; Boland, J. J.; Wang, J. J.; Donegan, J. F.; Grunlan, J. C.; Moriarty, G.; Shmeliov, A.; Nicholls, R. J.; Perkins, J. M.; Grieveson, E. M.; Theuwissen, K.; McComb, D. W.; Nellist, P. D.; Nicolosi, V. Two-Dimensional Nanosheets Produced by Liquid Exfoliation of Layered Materials. *Science* **2011**, *331* (6017), 568−571.

(21) Tamuly, P.; Sama, F.; Moorthy, J. N. Metal-Organic Nanosheets (MONs): Exfoliation by Mechanical Grinding and Iodine Capture. *Adv. Mater. Interfaces* **2022**, *9* (16), 2200337.
(22) Chaudhary, A.; Mohammad, A.; Mobin, S. M. Recent Advances in Single-Crystal-to-Single-Crystal Transformation at the Discrete Molecular Level. *Cryst. Growth Des.* **2017**, *17* (5), 2893−2910.
(23) Zeng, R.; He, T.; Lu, L.; Li, K.; Luo, Z.; Cai, K. Ultra-Thin Metal-Organic Framework Nanosheets for Chemo-Photodynamic Synergistic Therapy. *J. Mater. Chem. B* **2021**, *9* (20), 4143−4153.
(24) Qashqoosh, M. T. A.; Alahdal, F. A. M.; Manea, Y. K.; Zakariya, S. M.; Naqvi, S. Synthesis, Characterization and Spectroscopic Studies of Surfactant Loaded Antiulcer Drug into Chitosan Nanoparticles for Interaction with Bovine Serum Albumin. *Chem. Phys.* **2019**, *527*, 110462.
(25) Shimizu, T.; Nakano, Y.; Morimoto, S.; Tabata, T.; Hamaguchi, N.; Igari, Y. Formulation Study for Lansoprazole Fast-Disintegrating Tablet. I. Effect of Compression on Dissolution Behavior. *Chem. Pharm. Bull.* **2003**, *51* (8), 942−947.
(26) Shahnawaz Khan, M.; Khalid, M.; Shahid, M. What Triggers Dye Adsorption by Metal Organic Frameworks? The Current Perspectives. *Mater. Adv.* **2020**, *1* (6), 1575−1601.
(27) Khan, M. S.; Khalid, M.; Shahid, M. Engineered Fe 3 Triangle for the Rapid and Selective Removal of Aromatic Cationic Pollutants: Complexity Is Not a Necessity. *RSC Adv.* **2021**, *11* (5), 2630−2642.
(28) Qasem, K. M. A.; Khan, S.; Fitta, M.; Akhtar, M. N.; AlDamen, M. A.; Shahid, M.; Saleh, H. A. M.; Ahmad, M. A New $\{Cu_3\text{-}Gd_2\}$ Cluster as Two-in-One Functional Material with Unique Topology Acting as a Refrigerant as Well as Adsorbent for Cationic Dye. *CrystEngComm* **2022**, *24*, 5215−5225.
(29) Engvild, K. C. Chlorine-Containing Natural Compounds in Higher Plants. *Phytochemistry* **1986**, *25* (4), 781−791.
(30) Heibati, B.; Rodriguez-Couto, S.; Al-Ghouti, M. A.; Asif, M.; Tyagi, I.; Agarwal, S.; Gupta, V. K. Kinetics and Thermodynamics of Enhanced Adsorption of the Dye AR 18 Using Activated Carbons Prepared from Walnut and Poplar Woods. *J. Mol. Liq.* **2015**, *208*, 99−105.
(31) Song, B.; Wang, T.; Sun, H.; Shao, Q.; Zhao, J.; Song, K.; Hao, L.; Wang, L.; Guo, Z. Two-Step Hydrothermally Synthesized Carbon Nanodots/WO 3 Photocatalysts with Enhanced Photocatalytic Performance. *Dalt. Trans.* **2017**, *46* (45), 15769−15777.
(32) Freeman, H. S. Color Yes, Toxicity No: Systematic Approaches to Meeting This Challenge. *Colourage* **2005**, *52*, 59−65.
(33) Çınar, S.; Kaynar, Ü. H.; Aydemir, T.; Kaynar, S. C.; Ayvacıklı, M. An Efficient Removal of RB5 from Aqueous Solution by Adsorption onto Nano-ZnO/Chitosan Composite Beads. *Int. J. Biol. Macromol.* **2017**, *96*, 459−465.
(34) Kaur, H.; Kumar, R.; Kumar, A.; Krishnan, V.; Koner, R. R. Trifunctional Metal-Organic Platform for Environmental Remediation: Structural Features with Peripheral Hydroxyl Groups Facilitate Adsorption, Degradation and Reduction Processes. *Dalt. Trans.* **2019**, *48* (3), 915−927.
(35) Sonai, G. G.; de Souza, S. M. A. G. U.; de Oliveira, D.; de Souza, A. A. U. The Application of Textile Sludge Adsorbents for the Removal of Reactive Red 2 Dye. *J. Environ. Manage.* **2016**, *168*, 149−156.
(36) Xie, X.; Huang, J.; Zhang, Y.; Tong, Z.; Liao, A.; Guo, X.; Qin, Z.; Guo, Z. Aminated Cassava Residue-Based Magnetic Microspheres for Pb(II) Adsorption from Wastewater. *Korean J. Chem. Eng.* **2019**, *36* (2), 226−235.
(37) Ashafaq, M.; Khalid, M.; Raizada, M.; Ahmad, M. S.; Khan, M. S.; Shahid, M.; Ahmad, M. A Zn-Based Fluorescent Coordination Polymer as Bifunctional Sensor: Sensitive and Selective Aqueous-Phase Detection of Picric Acid and Heavy Metal Ion. *J. Inorg. Organomet. Polym. Mater.* **2020**, *30* (11), 4496−4509.
(38) Duo, H.; Tang, H.; Ma, J.; Lu, X.; Wang, L.; Liang, X. Iron-Based Metal-Organic Framework as an Effective Sorbent for the Rapid and Efficient Removal of Illegal Dyes. *New J. Chem.* **2019**, *43* (38), 15351−15358.
(39) Zhao, M.; Wang, Y.; Ma, Q.; Huang, Y.; Zhang, X.; Ping, J.; Zhang, Z.; Lu, Q.; Yu, Y.; Xu, H.; Zhao, Y.; Zhang, H. Ultrathin 2D Metal-Organic Framework Nanosheets. *Adv. Mater.* **2015**, *27* (45), 7372−7378.
(40) Ibers, J. A.; Hamilton, W. C. *International Tables for X-ray Crystallography*; Kynoch Press: Birmingham, England, 1974; Vol. *IV*.
(41) Ghosh, S. K.; Bharadwaj, P. K. Coordination Polymers of La(III) as Bunched Infinite Nanotubes and Their Conversion into an Open-Framework Structure. *Inorg. Chem.* **2005**, *44* (9), 3156−3161.
(42) Gupta, M.; Sahana, S.; Sharma, V.; Bharadwaj, P. K. Benzothiazole Integrated into a Cryptand for ESIPT-Based Selective Chemosensor for Zn2+ Ions. *Dalt. Trans.* **2019**, *48* (22), 7801−7808.
(43) Sheldrick, G. M. Crystal Structure Refinement with SHELXL. *Acta Crystallogr. Sect. C Struct. Chem.* **2015**, *71* (1), 3−8.
(44) Bourhis, L. J.; Dolomanov, O. V.; Gildea, R. J.; Howard, J. A. K.; Puschmann, H. The Anatomy of a Comprehensive Constrained, Restrained Refinement Program for the Modern Computing Environment - Olex2 Dissected. *Acta Crystallogr A Found Adv* **2015**, *71* (1), 59−75.
(45) Liao, W. M.; Zhang, J. H.; Yin, S. Y.; Lin, H.; Zhang, X.; Wang, J.; Wang, H. P.; Wu, K.; Wang, Z.; Fan, Y. N.; Pan, M.; Su, C. Y. Tailoring Exciton and Excimer Emission in an Exfoliated Ultrathin 2D Metal-Organic Framework. *Nat. Commun.* **2018**, *9* (1), 2401.
(46) Siepmann, F.; Eckart, K.; Maschke, A.; Kolter, K.; Siepmann, J. Modeling Drug Release from PVAc/PVP Matrix Tablets. *J. Controlled Release* **2010**, *141* (2), 216−222.
(47) Kalantzi, L.; Karavas, E.; Koutris, E.; Bikiaris, D. Recent Advances in Oral Pulsatile Drug Delivery. *Recent Pat. Drug Delivery Formul.* **2009**, *3* (1), 49−63.
(48) Pradhan, N. K.; Das, M.; Palve, Y. P.; Nayak, P. Synthesis and Characterization of Polylactic Acid/Cloisite 30B (MMT) Nanocomposite for Controlled Release of Anticancer Drug Curcumin. *Int. J. Pharm. Res. Allied Sci.* **2012**, *1* (4), 63−70.
(49) Raj, V.; Prabha, G. Synthesis, Characterization and in Vitro Drug Release of Cisplatin Loaded Cassava Starch Acetate-PEG/Gelatin Nanocomposites. *J. Assoc. Arab Univ. Basic Appl. Sci.* **2016**, *21*, 10−16.
(50) (a) Horcajada, P.; Serre, C.; Vallet-Regí, M.; Sebban, M.; Taulelle, F.; Férey, G. Metal-organic frameworks as efficient materials for drug delivery. *Angew. Chem.* **2006**, *45* (36), 5974−5978.
(51) Kim, M.; Boissonnault, J. A.; Allen, C. A.; Dau, P. V.; Cohen, S. M. Functional Tolerance in an Isoreticular Series of Highly Porous Metal-Organic Frameworks. *Dalt. Trans.* **2012**, *41* (20), 6277−6282.
(52) Taylor-Pashow, K. M. L.; Della Rocca, J.; Xie, Z.; Tran, S.; Lin, W. Postsynthetic Modifications of Iron-Carboxylate Nanoscale Metal-Organic Frameworks for Imaging and Drug Delivery. *J. Am. Chem. Soc.* **2009**, *131* (40), 14261−14263.
(53) Miller, S. R.; Heurtaux, D.; Baati, T.; Horcajada, P.; Grenèche, J. M.; Serre, C. Biodegradable Therapeutic MOFs for the Delivery of Bioactive Molecules. *Chem. Commun.* **2010**, *46* (25), 4526−4528.
(54) Huxford, R. C.; Della Rocca, J.; Lin, W. Metal-Organic Frameworks as Potential Drug Carriers. *Current Opinion in Chemical Biology.* **2010**, *14*, 262−268.
(55) Sun, C. Y.; Qin, C.; Wang, C. G.; Su, Z. M.; Wang, S.; Wang, X. L.; Yang, G. S.; Shao, K. Z.; Lan, Y. Q.; Wang, E. B. Chiral Nanoporous Metal-Organic Frameworks with High Porosity as Materials for Drug Delivery. *Adv. Mater.* **2011**, *23* (47), 5629−5632.
(56) Vishnyakov, A.; Ravikovitch, P. I.; Neimark, A. V.; Bülow, M.; Wang, Q. M. Nanopore Structure and Sorption Properties of Cu-BTC Metal-Organic Framework. *Nano Lett.* **2003**, *3* (6), 713−718.
(57) Lucena, F. R.; de Araújo, L. C.; Rodrigues, M. D.; da Silva, T. G.; Pereira, V. R.; Militão, G. C.; Rolim-Neto, P. J.; da Silva, F. F.; Nascimento, S. C.; Fontes, D. A. F. Induction of cancer cell death by apoptosis and slow release of 5-fluoracil from metal-organic frameworks Cu-BTC. *Biomed. Pharmacother.* **2013**, *67*, 707−713.
(58) Vora, C.; Patadia, R.; Mittal, K.; Mashru, R. Formulation Development, Process Optimization, and in Vitro Characterization of Spray-Dried Lansoprazole Enteric Microparticles. *Sci. Pharm.* **2016**, *84* (2), 393−408.

https://doi.org/10.1021/acsomega.2c08231
ACS Omega 2023, 8, 12232−12245

(59) Nagarajan, E.; Shanmugasundaram, P.; Ravichandiran, V.; Vijayalakshmi, A.; Senthilnathan, B.; Masilamani, K. Development and Evaluation of Chitosan Based Polymeric Nanoparticles of an Antiulcer Drug Lansoprazole. *J. Appl. Pharm. Sci.* **2015**, *5* (4), 20−25.
(60) Layre, A. M.; Gref, R.; Richard, J.; Requier, D.; Chacun, H.; Appel, M.; Domb, A. J.; Couvreur, P. Nanoencapsulation of a Crystalline Drug. *Int. J. Pharm.* **2005**, *298*, 323−327.
(61) Wu, W. P.; Wu, J.; Liu, J. Q.; Trivedi, M.; Kumar, A. Fabrication of a New Metal-Organic Framework for Sensitive Sensing of Nitroaromatics and Efficient Dye Adsorption. *RSC Adv.* **2017**, *7* (86), 54522−54531.
(62) Rajak, R.; Saraf, M.; Mohammad, A.; Mobin, S. M. Design and Construction of a Ferrocene Based Inclined Polycatenated Co-MOF for Supercapacitor and Dye Adsorption Applications. *J. Mater. Chem. A* **2017**, *5* (34), 17998−18011.
(63) Ahamad, M. N.; Khan, M. S.; Shahid, M.; Ahmad, M. Metal Organic Frameworks Decorated with Free Carboxylic Acid Groups: Topology, Metal Capture and Dye Adsorption Properties. *Dalt. Trans.* **2020**, *49* (41), 14690−14705.
(64) Qasem, K. M. A.; Khan, S.; Chinnam, S.; Saleh, H. A. M.; Mantasha, I.; Zeeshan, M.; Manea, Y. K.; Shahid, M. Sustainable Fabrication of Co-MOF@CNT Nano-Composite for Efficient Adsorption and Removal of Organic Dyes and Selective Sensing of Cr(VI) in Aqueous Phase. *Mater. Chem. Phys.* **2022**, *291*, 126748.
(65) Alqadami, A. A.; Naushad, M.; Alothman, Z. A.; Ahamad, T. Adsorptive Performance of MOF Nanocomposite for Methylene Blue and Malachite Green Dyes: Kinetics, Isotherm and Mechanism. *J. Environ. Manage.* **2018**, *223*, 29−36.
(66) Ahmad, M. S.; Khalid, M.; Khan, M. S.; Shahid, M.; Ahmad, M. Exploiting One Dimensional Polymer for Environmental Monitoring: Co Based Coordination Polymer for Efficient Removal of Cationic Dyes. *J. Solid State Chem.* **2022**, *313*, 123307.
(67) Hu, F. L.; Shi, Y. X.; Chen, H. H.; Lang, J. P. A Zn(II) Coordination Polymer and Its Photocycloaddition Product: Syntheses, Structures, Selective Luminescence Sensing of Iron(III) Ions and Selective Absorption of Dyes. *Dalt. Trans.* **2015**, *44* (43), 18795−18803.
(68) Dalapati, R.; Kökçam-Demir, D. C.; Janiak, C.; Biswas, S. The Effect of Functional Groups in the Aqueous-Phase Selective Sensing of Fe(III) Ions by Thienothiophene-Based Zirconium Metal-Organic Frameworks and the Design of Molecular Logic Gates. *Dalt. Trans.* **2018**, *47* (4), 1159−1170.
(69) Xiao, L.; Xiong, Y.; Tian, S.; He, C.; Su, Q.; Wen, Z. One-Dimensional Coordination Supramolecular Polymer [Cu(Bipy)-(SO4)]n as an Adsorbent for Adsorption and Kinetic Separation of Anionic Dyes. *Chem. Eng. J.* **2015**, *265* (1), 157−163.
(70) Li, J. J.; Wang, C. C.; Fu, H. F.; Cui, J. R.; Xu, P.; Guo, J.; Li, J. R. High-Performance Adsorption and Separation of Anionic Dyes in Water Using a Chemically Stable Graphene-like Metal-Organic Framework. *Dalt. Trans.* **2017**, *46* (31), 10197−10201.
(71) Hassan, S. M.; Ibrahim, A. A.; Mohamed, D. A. Adsorption of Anionic and Cationic Dyes from Aqueous Solutions by Metal Organic Frameworks: Equilibrium and Kinetics Study. *Int. J. Mod. Chem.* **2017**, *2017* (1), 111−126.
(72) Ahmad, N.; Younus, H. A.; Chughtai, A. H.; Van Hecke, K.; Khattak, Z. A. K.; Gaoke, Z.; Danish, M.; Verpoort, F. Synthesis of 2D MOF Having Potential for Efficient Dye Adsorption and Catalytic Applications. *Catal. Sci. Technol.* **2018**, *8* (16), 4010−4017.
(73) Mantasha, I.; Hussain, S.; Ahmad, M.; Shahid, M. Two Dimensional (2D) Molecular Frameworks for Rapid and Selective Adsorption of Hazardous Aromatic Dyes from Aqueous Phase. *Sep. Purif. Technol.* **2020**, *238*, 116413.
(74) Xu, J.; Zhuo, Q.; Fu, R.; Cheng, H.; Tang, X.; Ma, Y.; Xie, J.; Yuan, R. A 2D Metal-Organic Framework for Selective Adsorptions on Organic Dyes. *Inorg. Chim. Acta* **2016**, *446*, 198−202.
(75) Patel, U.; Parmar, B.; Patel, P.; Dadhania, A.; Suresh, E. The Synthesis and Characterization of Zn(Ii)/Cd(Ii) Based MOFs by a Mixed Ligand Strategy: A Zn(Ii) MOF as a Dual Functional Material for Reversible Dye Adsorption and as a Heterogeneous Catalyst for the Biginelli Reaction. *Mater. Chem. Front.* **2021**, *5* (1), 304−314.
(76) Gong, H.; Li, Y.; Li, H.; Jin, Z. 2D CeO2 and a Partially Phosphated 2D Ni-Based Metal-Organic Framework Formed an S-Scheme Heterojunction for Efficient Photocatalytic Hydrogen Evolution. *Langmuir* **2022**, *38* (6), 2117−2131.

https://doi.org/10.1021/acsomega.2c08231
ACS Omega 2023, 8, 12232−12245